Comparative simulation study of the structure of the plastic zone produced by nanoindentation

Yu Gao [a], Carlos J. Ruestes [b], Diego R. Tramontina [b,c], Herbert M. Urbassek [a,*]

[a] *Fachbereich Physik und Forschungszentrum OPTIMAS, Universität Kaiserslautern, Erwin-Schrödinger-Straße, D-67663 Kaiserslautern, Germany*
[b] *Facultad de Ciencias Exactas y Naturales, Universidad Nacional de Cuyo, Mendoza M5502JMA, Argentina*
[c] *Instituto de Bioingeniería, Universidad de Mendoza, Mendoza M5502BZG, Argentina*

ARTICLE INFO

ABSTRACT

Using molecular-dynamics simulation, we study nanoindentation in fcc (Cu and Al) and bcc (Fe and Ta) metals by a spherical indenter and investigate the size of the plastic zone generated. We find that while it does not strongly depend on crystal structure, surface orientation, and indentation parameters, the extent of the plastic zone is substantially larger before the retraction of the indenter. After retraction, the results are in good agreement with available published data. Plasticity develops by the generation, propagation and reaction of dislocations; they fall into two groups, those that adhere to the indentation pit, and those that have been emitted either into the substrate interior or glide along the surface. The total length of the dislocation network generated roughly follows available geometrical estimates; results for individual surface orientations may, however, differ quite strongly. The radial distribution of the dislocations attached to the indentation pit is computed; as a rule it shows a maximum at some depth below the indentation pit.

© 2014 Elsevier Ltd. All rights reserved.

1. Introduction

Indentation constitutes a prototypical example where the creation of plasticity can be studied (Tabor, 1951; Johnson, 1985; Fischer-Cripps, 2004). Consider for concreteness a spherical indenter of radius R which is pushed into the surface to a depth d. For small depths d, the deformation of the surface is purely elastic. With increasing d, the pressure generated in the substrate rises, until it surpasses the yield strength of the material and dislocations nucleate. This occurs inside the material at some distance from the indenter. The generated dislocations move away from the indenter due to the strong stress gradient produced. The region filled with dislocations is known as the *plastic zone*; the determination of its size and properties is the topic of this paper.

Besides fundamental interest in the properties of the plasticity generated, the dislocations contained in it influence the properties of the material. In particular they lead to work hardening of the material; its magnitude depends on the dislocation density in the plastic zone and thus of its size. This effect is well known in the literature as the *indentation size effect* (Nix and Gao, 1998): the indentation hardness measured in an indentation experiment depends on the indentation depth. The determination of the dislocation density in the plastic zone is a key input parameter to quantify this hardening (Nix and Gao, 1998).

Early studies of indentation – summarized in Johnson (1985) – were based on the simple model of an elastic–plastic solid: the solid responds elastically to pressures up to the yield strength and deforms plastically for higher pressures. A convenient length scale is given by the *contact radius a_c*; it is the radius of the (circular) contact region between indenter and substrate, projected onto the surface plane, and is easily accessible to experiment. For a spherical indenter of radius R indented to a depth d, it is

$$a_c = \sqrt{R^2 - (R - d)^2}. \tag{1}$$

These isotropic continuum-mechanical studies find that the plastic zone is roughly hemispherical; its radius R_{pl} scales with the contact radius as

$$R_{pl} = fa_c. \tag{2}$$

The *plastic-zone size factor f* is of the order of $f = 2$–3, as can for instance be read off Figs. 6.15 and 6.16 in Johnson (1985). In a recent investigation, Durst et al. (2005) corroborated these numerical calculations and state that the plastic-zone size factor f depends on the material and ranges from 0 to around 3.5. In this paper they studied experimentally Cu and found the value of $f = 1.9$.

In the following years, several further investigations on the size of the plastic zone were published. Yang and Vehoff (2007) deduced a value of $f = 3.5$ for Ni. Graca et al., however, again adopted the value of $f = 1.9$ – as obtained by Durst et al. for Cu – for their Ni study (Graca et al., 2008). In parallel, Cao et al. deduced $f = 1.74$ to adjust their model to the experimental values of Huang et al. (2000) for Cu (Cao et al., 2008). A year later, Chicot compared nano- and microindentation hardness and suggested $f = 1.44$ independently of the substrate material (Chicot, 2009). Continuing in chronological order, Qiao et al. required f to be flexible in order to be able to compare with different models and data (Qiao et al., 2010). More recently Begau et al. (2012) again used a fixed value of $f = 1.9$ and quoted (Hua and Hartmaier, 2010) who previously took it from (Durst et al., 2005).

It should be noted that previously the size of the plastic zone was denoted as the so-called c/a ratio (Gerberich et al., 2002); since $c = R_{pl}$ denotes the radius of the plastic zone, and $a = a_c$ the contact radius, $f = c/a$. This ratio is also closely connected to the so-called surface-volume ratio – the ratio of the area of the contact surface, πa_c^2, to the volume of the plastic zone, $(2\pi/3)R_{pl}^3$ – which was also considered a key parameter describing indentation-induced plasticity (Gerberich et al., 2002).

This compilation demonstrates that the appropriate choice of the size of the plastic zone is under vivid discussion and an independent means of clarifying its magnitude is needed. The plastic-zone size is not only relevant to the constitutive modeling community but also to experimentalists. The direct experimental determination of f is possible but non-trivial. It requires nanoindentation on single crystals, cutting the indented volume out of the substrate and performing a TEM analysis in order to determine dislocation structures and densities. An alternative approach is provided by molecular dynamics (MD) simulations and will be followed here.

Besides the size of the plastic zone, the total length of dislocations stored in it, L_{disl}, is important. Its knowledge allows to calculate the (average) dislocation density, $\bar{\rho}$, as

$$\bar{\rho} = \frac{L_{disl}}{V_{pl}}. \tag{3}$$

Here the volume of the plastic zone is obtained from

$$V_{pl} = \frac{2\pi}{3}R_{pl}^3 - V_{indent}, \tag{4}$$

where the volume of the immersed part of the indenter, V_{indent}, is subtracted from the hemispherical plastic-zone volume.

Hardening models – such as the venerable Taylor model (Taylor, 1934, 1934; Abbaschian et al., 2010) – use the density of generated dislocations as important input. In the Taylor model, the yield stress depends on the dislocation density as

$$Y = \alpha Gb \sqrt{\bar{\rho} + \rho_0}, \tag{5}$$

where α is a dimensionless number of order $1/2$, G is the shear modulus, and b is the Burgers vector. ρ_0 denotes the background dislocation density – present in the material before indent – and $\bar{\rho}$ as above its increase due to the indentation-generated dislocations. This model is used to calculate the hardness increase for shallow indentations (indentation-size effect) (Nix and Gao, 1998; Durst et al., 2005).

The total length of dislocations produced during indent has first been calculated by Nix and Gao (1998) for a conical indenter and by Swadener et al. (2002) for a spherical indenter (in a paraboloid approximation). These studies assume that the dislocations generated are prismatic dislocation loops with Burgers vector directed downward perpendicular to the initial substrate surface. The number and length of these loops can be calculated from a simple geometric argument, by integrating up the number of steps necessary to reduce the indented surface. For a spherical indenter these considerations give

$$L_{\text{disl}} = \frac{2\pi}{3} \frac{a_c^3}{bR}$$

(6)

and

$$\bar{\rho} = \frac{1}{bRf^3},$$

(7)

if the correction by V_{indent} is ignored. Thus, for a spherical indenter the dislocation density does not depend on indentation depth d, but only on the radius of the indenter.

The dislocations proposed in the Nix–Gao approach are termed *geometrically necessary dislocations*, to contrast them from other – so-called statistically stored – dislocations. In later work (Gao et al., 1999) these authors use these concepts to construct a mesoscale theory of strain-gradient plasticity. Arsenlis and Parks (1999) argue that – due to crystallinity effects not taken into account by Nix and Gao – the true number of geometrically necessary dislocations must be larger than in Eq. (6); the corresponding correction is provided by the Nye factor and assumes a value of around 2 (Swadener et al., 2002). Hua and Hartmaier (2010), on the other hand, calculate dislocation lengths using MD simulation for a specific case, an $R=8$ nm indenter into a Cu (111) surface. They calculate the so-called vectorial dislocation densities by weighting each (piece of a) dislocation line by its Burgers vector; in this way, dislocations with opposing Burgers vector cancel in the summation. The authors argue that this definition is identical with that of geometrically necessary dislocations. In view of the uncertainties in the various definitions of dislocations, we will monitor all dislocations produced during indentation. In later work, Engels et al. (2012) extend the knowledge obtained by atomistic simulations to a mesoscopic model of crystal plasticity based on the dislocation density. This allows them to include in particular preexisting dislocations into the description. In a related study, Begau et al. (2012) explore methods to extract information on the local dislocation density tensors calculated on an atomic level from MD simulations; such data can help bridge atomistic simulations and continuum descriptions.

After the pioneering work of Nix and Gao (1998), several extensions to this model have been published. Al-Rub and Voyiadjis (2004) explore the connection of the theory of geometrically necessary dislocations and strain gradient plasticity theory, where they focus on the proper coupling between the statistically stored and the geometrically necessary dislocations during indentation. Later, Faghihi and Voyiadjis (2012) extend these ideas and include also temperature and rate dependent indentation size effects for the particular case of bcc solids. Qu et al. (2004) investigate the effect of the indenter tip radius on indentation of spherical, conical and cono-spherical indenters using finite-element models. Later they provide a model for nanoindentation of spherical indenters (Qu et al., 2006) which is extended to the nano-scale by Huang et al. (2007). Kim et al. (2005) improve the original Nix–Gao model by including a rounded tip in the conical indenter. Pugno (2007) extends the Nix–Gao model to general indenter shapes. Muraishi (2013) describes the indentation by a Berkovich indenter using triangular dislocation loops. Finally, Cordill et al. (2009) study cyclic loading, also known as dynamic indentation. They find that dynamic loading produces more dislocations than in a single indentation.

Both the (isotropic) continuum theory of the generation of the plastic zone and the model based on geometrically necessary dislocations to calculate the dislocation length take crystal effects not or only incompletely into account; they are therefore better suited to describe indentation into a polycrystal than into single-crystalline substrates. For nanoindentation, however, often the selective indentation into a single grain is possible. Therefore the question arises in how far the size of the plastic zone and the dislocation density generated depend on the crystallinity and surface orientation of the material.

Recently continuum models of crystal plasticity were developed which take the crystalline anisotropy into full account. They allow one to study the activation of slip systems at different stages of indentation, the influence of crystal orientation, the deformation patterns around the indent, and even the distribution of dislocations inside the indented material (Wang et al., 2004; Zaafarani et al., 2008; Zambaldi and Raabe, 2010; Reuber et al., 2014; Yao et al., 2014). Both indentations into fcc and bcc crystals have been treated by this method. In contrast to isotropic continuum models used earlier (Johnson, 1985) these models predict anisotropic surface patterns and also anisotropic plastic zones.

An alternative theoretical approach is provided by atomistic simulation. Molecular dynamic simulations allow to follow the indentation process and offer the advantage of obtaining an atomistic picture of the plastic zone generated, including many details of dislocation generation, reaction and annihilation. Such simulations have nowadays been performed for many materials, in particular fcc and bcc metals (Van Vliet et al., 2003; Ma and Yang, 2003; Zhu et al., 2004; Liang et al., 2004; Asenjo et al., 2006; Tsuru and Shibutani, 2007; Ju et al., 2007; Carrasco and Rodrìguez de la Fuente, 2008; Ziegenhain et al., 2010; Paul et al., 2013; Hagelaar et al., 2006; Biener et al., 2007; Alcalá et al., 2012; Christopher et al., 2001; Smith et al., 2003; Lu et al., 2009a,b; Kumar et al., 2013; Gao et al., 2014). MD has played a major role in identifying the processes of dislocation nucleation and slip and allows to correlate experimentally measured features in the load–displacement curves with their atomistic origin (Gouldstone et al., 2007). Effects of surface crystallinity are naturally included. At the same time, the limitations of the atomistic simulation have been early recognized and characterized. (i) The length scale of roughly up to around 100 nm is not critical as tip sizes used in experiment have been continuously decreasing and now tips with 50 nm radius are available. (ii) A more important problem is the time scale. Simulations model indentations with speeds of usually 1 m/s and above, while experiments are at 1 μm/s and below; the record minimum indentation velocity in MD appears to be Alcalá et al. (2012) with 4 mm/s in Ta. At low penetration speeds, thermally activated processes have more time to develop as they overcome the rate-limiting activation barriers. These are not included in conventional MD; accelerated MD

techniques (Voter et al., 2002) have to our knowledge not yet been applied to the problem of nanoindentation. In this sense, MD refers to the 'athermal limit' of the plasticity processes (Van Vliet et al., 2003). In their review of the role of atomistic simulation of mechanical behavior, Li et al. (2003) point out that atomistic nanoindentation simulations provided important insights on the strength of materials, homogeneous defect nucleation and incipient plasticity. We note that the theoretical analysis of the rate dependence of nanoindentation constitutes a non-trivial problem (Wo et al., 2005; Mason et al., 2006). (iii) Finally, MD simulations are often – as in the present paper – performed in ideal, defect-free solids. Preexisting defects, may, however, change the dislocation nucleation rate by allowing for heterogeneous nucleation processes. This last caveat seems less severe for small indenters, since here the number of defects found in the relevant volume will be small. While we are not aware of studies relating the size of the plastic zone to the amount of pre-existing defects in the substrate, it is known that dislocation nucleation is definitely affected by such defects. Already in 1998, Kiely et al. (1998) remarked that surface imperfections – such as steps – influence dislocation nucleation, as they observed in experiment that dislocations nucleate at smaller loads close to steps than on a perfect terrace. Later Zimmerman et al. (2001) demonstrated this effect using MD simulation. The same influence was found near grain boundaries (Lilleodden et al., 2003) and on adatom islands (Ziegenhain and Urbassek, 2010).

In the present paper, we shall use the technique of molecular-dynamics simulation to systematically study the properties of the plastic zone generated by indentation; the size of the plastic zone, the total length of dislocations, and the dislocation density will be analyzed. The effects of substrate crystal structure (bcc or fcc) and surface orientation (along the 3 low-indexed surfaces) will be investigated. In addition we asses the influence of indenter radius, target temperature and indentation velocity.

2. Method

2.1. Simulation

The MD simulations are performed using the open-source LAMMPS code (Plimpton, 1995) with a constant time step of 1 fs. We use two indenter sizes: $R=2.14$ nm, called the small indenter, and $R=10$ nm, called the large indenter. Unless otherwise noted the method and the results apply to the small indenter.

Fig. 1 shows a schematic representation of the MD simulation system. It illustrates the configuration of the nanoindenter and the substrate crystal. Our simulation consists of two parts: (i) nanoindentation, during which the indenter is pushed in the z direction into the substrate; and (ii) retraction of the indenter: the indenter is moved out of the substrate to return to the initial height.

We study indentation into two fcc metals (Al and Cu) and two bcc metals (Fe and Ta). In all cases, the substrate is a single crystal; the three low-indexed surface orientations – (100), (110), and (111) – are studied.

The substrate interactions are chosen as follows. The Fe–Fe interaction is described by the Mendelev potential (Mendelev et al., 2003). For Al we use the potential developed by Mendelev et al. (2008), for Cu the Mishin et al. potential (Mishin et al., 2001), and for Ta the Dai et al. potential (Dai et al., 2006). These potentials are all many-body potentials of the embedded-atom-model (EAM) type. We note that the choice of an appropriate interatomic interaction potential is essential for the
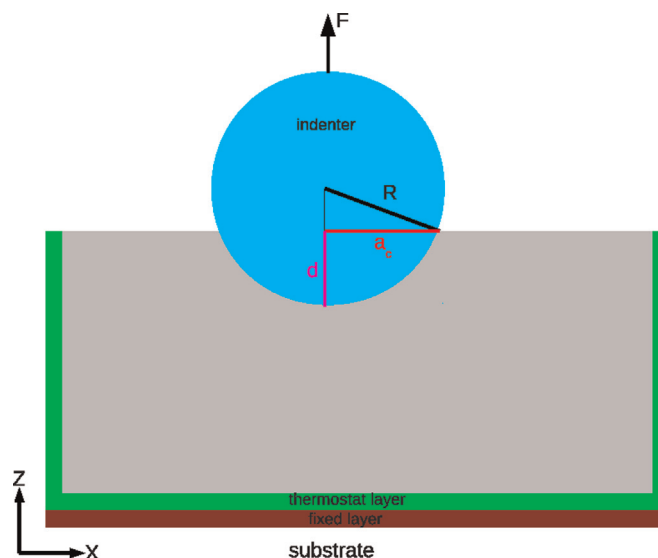

Fig. 1. Setup of the simulation system. The radius R of the indenter, its indentation depth d, the contact-area radius a_c and the indentation force F are indicated. The substrate has thermostatting and rigid zones at its boundaries.

quality of the MD results. The potentials available for indentation studies in Ta have been characterized recently (Ruestes et al., 2014); it has been found that among the available potentials (Li et al., 2003; Ravelo et al., 2012, 2013) the potential by Dai et al. (2006) fares best. Differences among the performance of the potentials could be traced back to the pressure dependence of the calculated elastic constants as well as the reliability of the stacking-fault energy surfaces.

For Fe, a recent study compares in detail the dislocation core structure, the core energy, and the Peierls stress (Gunkelmann et al., 2012). Among the 4 different potentials compared (Harrison et al., 1989; Mendelev et al., 2003; Lee et al., 2012; Gunkelmann et al., 2012) the Mendelev et al. potential (Mendelev et al., 2003) describes Fe dislocations most faithfully. A recent review (Malerba et al., 2010) analyzes the applicability of several Fe potentials to describe defect properties and also concludes that Mendelev-type potentials are currently the best choice to describe defects in Fe.

Another study compares the performance of EAM potentials compared to pair potentials specifically for nanoindentation (Ziegenhain et al., 2009). For the case of Cu these authors find that even pair-potentials qualitatively reproduce well many features of nanoindentation. Quantitatively their main deficits lie in their inflexibility to implement the elastic anisotropy of cubic crystals, and in particular in a gross underestimation of the stable stacking fault energy. As a consequence pair potentials predict the formation of too large dislocation loops, the too rapid expansion of partials, too little cross slip and in consequence a severe overestimation of work hardening.

The small indenter has a spherical shape with a radius of $R=2.14$ nm. It consists of 7248 C atoms arranged in a diamond lattice structure. It is rigid during the simulation; i.e., all C atoms move as a rigid body. The interaction between the indenter and the substrates is modeled by a purely repulsive potential; this is obtained from a Lennard–Jones potential (Banerjee et al., 2008), which is cut-off at 4.2 Å at its minimum and then shifted such as to have continuous energy and force at the cut-off radius.

The substrates comprise between 1 and 4 million atoms, depending on the material and the surface orientation. Typical dimensions are 20–40 nm in each direction. We checked that the simulation box is large enough to avoid that the generated dislocations reach the boundaries of the simulation box. Two atom layers at the bottom are fixed in order to suppress any rigid-body movement of the substrate. The next four layers at the bottom, as well as the outermost four layers of the substrate in lateral directions are kept at a fixed temperature $T=0$ K by velocity scaling. In addition, periodic boundary conditions are applied in the lateral x and y directions. The top surface is free.

Before performing the nanoindentation simulations, the substrates are relaxed until all stress components have reached values $<10^{-5}$ GPa (Ziegenhain et al., 2010). The center of the indenter is placed at a height of 2.6 nm above the substrate surface such that all indenter atoms are outside the cut-off range of the Fe–C interaction potential. After that the nanoindentation simulations are performed. The indenter moves with a constant velocity v; we chose $v=20$ m/s except in the Appendix. After indentation the indenter is retracted from the substrate; here a higher velocity, $v=100$ m/s was adopted; we performed test simulations with a smaller retraction velocity, $v=20$ m/s, but this alters the results only negligibly. The simulation is performed in the so-called velocity-controlled way; that is, at every MD time step Δt, the indenter proceeds rigidly by a path length $v \cdot \Delta t$. The indenter penetrates the substrate until a depth d; we penetrate up to a maximum depth of $R=2.14$ nm, equal to the indenter radius. The retraction process is simulated analogously to the indentation.

In addition to the systems described above we perform simulations with a larger indenter (radius $R=10$ nm) in a larger substrate. The sample is relaxed as described above and then thermostated to a temperature of 300 K using a Nosé–Hoover thermostat. In addition, we perform simulations at 10 K in order to be able to assess the effect of the sample temperature, see the Appendix. The indenter is modeled as a rigid indenter and the interaction with the substrate is described by a repulsive force as in Kelchner et al. (1998). Indentation proceeds with a velocity of 34 m/s, which is only 1% of the sound speed for Ta. The indenter penetrates to a depth of 2/3 of the indenter radius. The substrate consists of Ta crystals of size $50 \times 50 \times 40$ nm^3 (around 6 million atoms); crystals with surfaces in the three principal orientations – namely (100), (110) and (111) – are studied.

2.2. Detection algorithms and calculation of dislocation density

In order to identify the lattice dislocations and to determine their Burgers vectors, the Dislocation Extraction Algorithm (DXA) is used (Stukowski and Albe, 2010). It is based on the Common Neighbor Analysis (CNA) method (Faken and Jonsson, 1994) and allows to identify the local crystallographic structure in the neighborhood of each atom. Dislocation cores are identified by performing Burgers circuits and shrinking them as far as possible. The positions of the dislocation cores are used to construct the one-dimensional dislocation lines. This allows both to calculate the number of dislocations and to measure the length of dislocation lines, L_{disl}. Note that DXA measures the length of dislocation lines irrespective of their nature; in particular every Shockley partial contributes to L_{disl}. This must be kept in mind since theoretical models as presented in Section 1 do not consider the splitting of full dislocations into partials. In addition, the Crystal Analysis Tool (CAT) (Stukowski et al., 2012; Stukowski, 2012; Stukowski and Arsenlis, 2012) is employed to identify particular defects, such as twins. For visualization of the atomistic configurations we use the free software tools Atomeye (Li, 2003), ParaView (Henderson, 2007) and the Open Visualization Tool OVITO (Stukowski, 2010).

We identify the plastic zone as follows. The atomistic configurations after full penetration and after complete retraction are analyzed by means of DXA (Stukowski and Albe, 2010). From these analyses we find the configuration of the dislocation lines such as they are presented in the snapshots below. The dislocations fall into two groups: (i) those that still adhere to the imprint surface, and (ii) closed dislocation loops that have been pushed out of the indentation volume, either along the
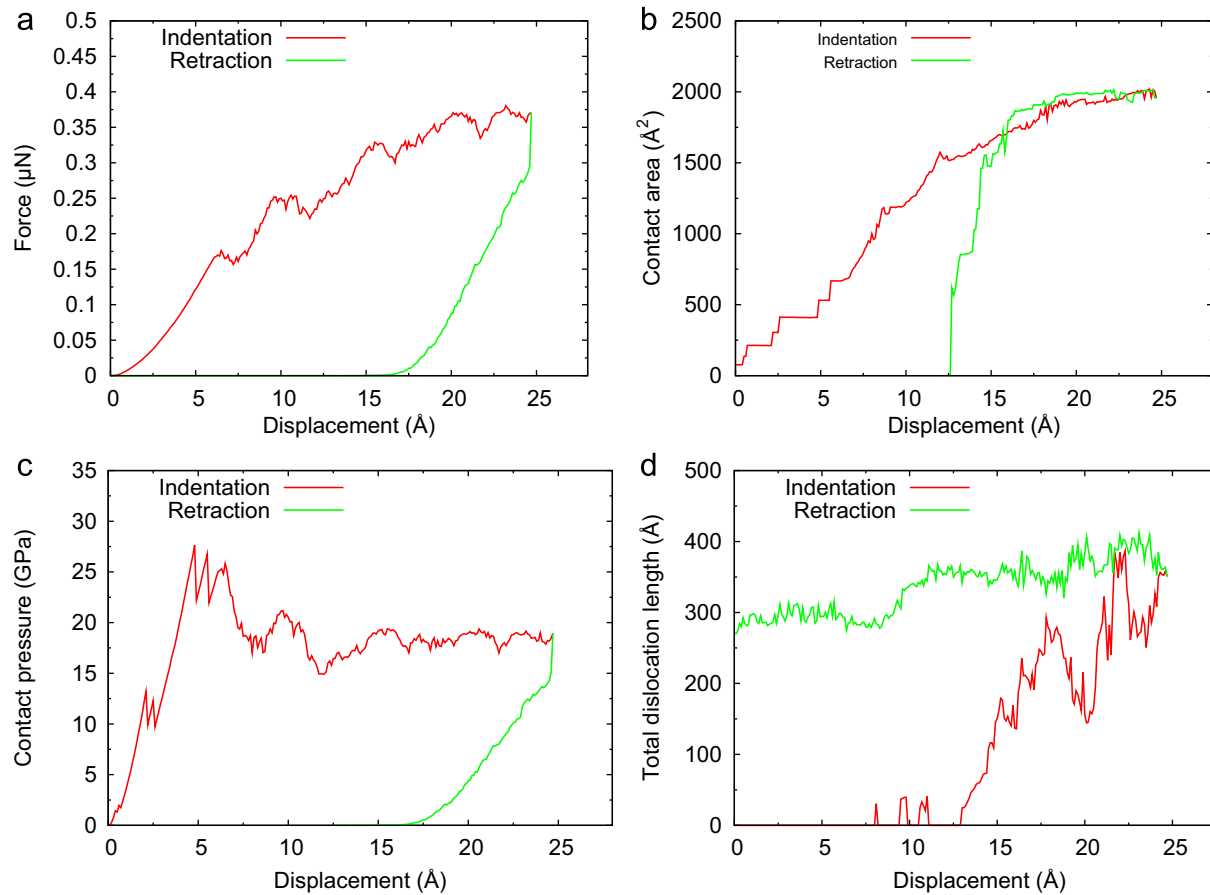
Fig. 2. Evolution of (a) normal force, (b) contact area, (c) contact pressure and (d) total dislocation length during the indentation and retraction process. Data obtained for indentation with an indenter of $R=2.14$ nm radius into the Ta (100) surface at 0 K. The abscissa scale has been normalized such that the interaction between indenter and surface starts at zero displacement.
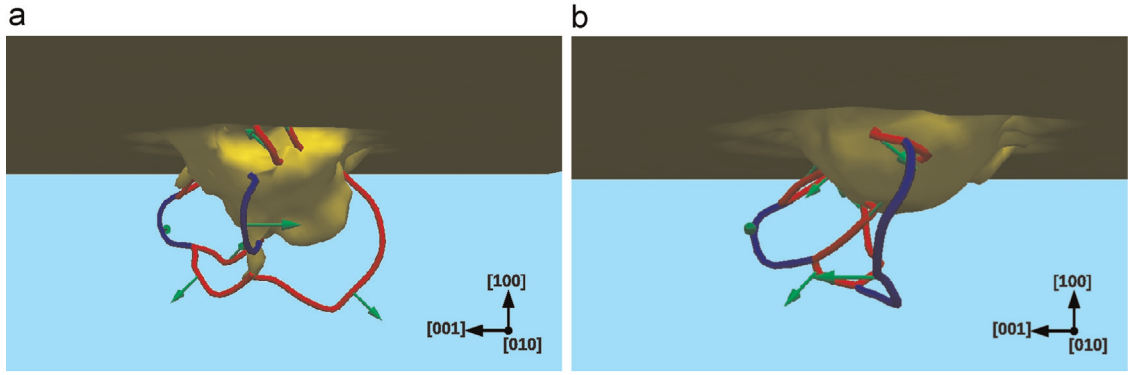
Y. Gao et al. / J. Mech. Phys. Solids 75 (2015) 58–75

63

Fig. 3. Snapshots showing defect formation (a) after indent and (b) after retraction of the indenter (radius 2.14 nm) into the Ta (100) surface at 0 K. Yellow: deformed surface including unidentified defects. Dislocation lines with Burgers vector $b = \frac{1}{2}\langle 111 \rangle$ are shown in red, those with $b = \langle 100 \rangle$ in blue. Green arrows indicate direction of b. Dislocations are detected using the DXA algorithm (Stukowski and Albe, 2010). Visualization has been prepared using Paraview (Henderson, 2007). (For interpretation of the references to color in this figure caption, the reader is referred to the web version of this article.)

surface or deeper into the simulation volume. We restrict our attention to dislocations of type (i) that still adhere to the imprint surface for the following reasons. (a) Experimentally, dislocations of type (ii) cannot be unambiguously assigned to be caused by the indenter, since they might have been present in the substrate already before indentation. Our definition that includes only dislocations (i) adherent to the imprint surface thus corresponds to the experimental procedure. (b) Once loops got detached from the indented zone they can easily move far away from the imprint surface. For the example of Ta, we find that detached loops propagate very easily in a pencil-glide fashion (Hull and Bacon, 1984); moreover, their propagation speed and the distance covered are strongly influenced by the indenter velocity. Also previous simulations of indentation into Al (111) (Lee et al., 2005) show significant prismatic-loop gliding once the loops become detached from the indent-originating network. The strong sensitivity of the distance covered by loops of type (ii) on simulation details (such as the simulation volume) and on physical parameters (such as the indent velocity) also indicate that they are no appropriate measure of the plastic zone.

We determine the largest distance R_{pl} of the dislocations that still adhere to the imprint surface from the center of the indenter; this R_{pl} is called the *radius of the plastic zone*. The volume of the plastic zone is considered to be of hemispherical form and is obtained by Eq. (4). The (average) density of dislocations, $\bar{\rho}$, is then evaluated by Eq. (3).

In addition, following Hua and Hartmaier (2010), local dislocation densities, $\rho(r)$, are computed. This is achieved by processing the DXA output by an in-house code which defines hemispherical shells and computes the dislocation density within the selected shells; their thickness was chosen as 10 Å for the small indenter and 16 Å for the large indenter. The average dislocation density in the plastic zone then satisfies

$$\bar{\rho} = \frac{1}{V_{pl}} \int_{a_c}^{R_{pl}} 4\pi r^2 \rho(r)\, dr. \tag{8}$$

The force on the indenter, F, is determined as the sum of the forces exerted by all substrate atoms on the indenter in the z direction, perpendicular to the surface. The force is purely repulsive since also the indenter–substrate interaction in our model is purely repulsive. The contact pressure is defined as the ratio of the indentation force F and the projected contact area A_c,

$$p_c(d) = \frac{F(d)}{A_c(d)}. \tag{9}$$

The contact area is determined from the x and y coordinates of the Fe atoms that are in contact with (that is, within the interatomic potential cut-off radius of 4.2 Å of) the indenter. A_c is calculated from an elliptical approximation to the set of these contact atoms, see Ziegenhain et al. (2010).

3. Results

3.1. Exemplary discussion: Ta (100)

In this section we provide an overview of the characteristics of the indentation-induced plastic zone by concentrating on one particular case, the indentation of the Ta (100) surface with the 2.14 nm indenter. Fig. 2 displays the basic results of the indentation process: indentation force, contact area and pressure and the evolution of the length of the dislocation network. Both the results during the indentation and during the retraction process are presented.
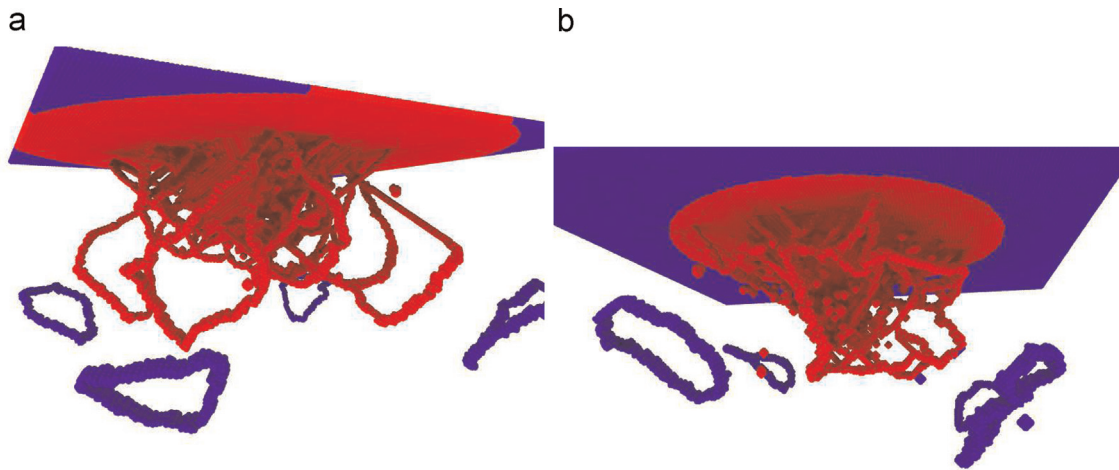
Fig. 4. Snapshots showing defect formation (a) after indent and (b) after retraction of the indenter (radius 10 nm) into the Ta (100) surface at 300 K, indented to $d = R/3$. Atoms inside the plastic zone (radius R_{pl} = 30.6 nm after indent and R_{pl} = 19.5 nm after retraction, see Table 2) are plotted red; outside blue. Dislocations are detected using the Crystal Analysis Tool (CAT) (Stukowski et al., 2012; Stukowski, 2012; Stukowski and Arsenlis, 2012). Visualization has been prepared using OVITO (Stukowski, 2010). (For interpretation of the references to color in this figure caption, the reader is referred to the web version of this article.)

Let us first discuss the generation of dislocations during the indentation process. The force, Fig. 2(a), and the contact area, Fig. 2(b), start increasing as soon as the indenter comes into contact with the surface. The force F initially follows the Hertzian $d^{3/2}$ increase as a function of indentation depth d; this is the signature of the elastic regime, where pressures are too small to generate dislocations. The contact pressure, Fig. 2(c), initially increases strongly with indentation depth, until the generation of dislocations, Fig. 2(d), at an indentation depth of around 7 Å relieves the pressure. Small fluctuations in the pressure – but not the force – are seen at a depth of around 3 Å; these are caused by abrupt increases of the contact area, Fig. 2(b), which let the contact pressure, Eq. (9), decrease. Fluctuations in the force curve, Fig. 2(a), and – even more pronouncedly – in the pressure, Fig. 2(c), indicate the nucleation of dislocations below the surface. As Fig. 2(d) shows such dislocations are first generated at an indentation depth of 7 Å. Also later, dislocations are produced in bursts, where the dislocation length suddenly increases; analogously dislocation reactions, which simplify the network, are visible at larger indentation depths, where the network length suddenly shrinks. The dislocation bursts are visible as small force fluctuations in the force curve, Fig. 2(a), and in the pressure, Fig. 2(c). The generation of dislocations relieves the pressure on the indenter such that it reaches a plateau value after indentation depths of ~15 Å; this value defines the hardness of the material. Also the force levels off towards larger indentation depths $d \sim R$, since the contact area changes little at these depths. When the indenter reaches maximum indentation, $d = R$, the force has roughly reached a constant value of 0.37 μN. We note that if the indenter is held for a while at the point of maximum indentation, the generated dislocation network relaxes somewhat; in test simulations we found changes of around 10 % both in the total dislocation length and in the radius of the plastic zone.

Upon retraction, both force and pressure decrease again; this decrease proceeds first rather abruptly due to the sudden change of the direction of the indenter velocity. Interestingly this decrease is first accompanied by a slight increase of the total length of the dislocation network. We assume that this is due to the fact that the still expanding dislocations still keep moving outward even while the indenter retracts; this is an effect of the dislocation inertia. The further retraction leads, however, to a more or less continuous decrease of the total dislocation length; again this decrease is characterized by abrupt length changes reflecting – besides the motion of dislocations – their reactions that lead to a re-organization of the network. These changes in the structure of the plastic zone are also reflected by small wiggles in the force and pressure curves. The indenter loses contact with the substrate at around $d = 17$ Å; upon further retraction both the force on the indenter and the contact pressure vanish. However, the substrate has not yet relaxed to an equilibrium; the dislocation network keeps re-organizing until the end of the simulation. These final changes appear minor so that we can consider the final situation as more or less relaxed.

Upon retraction the force vanishes at 17 Å. This is the depth of the indent pit; it is slightly smaller than the indentation depth of 21.4 Å. The pit surface has moved somewhat outward during the retraction of the indenter, due to relaxation processes in the material.

Fig. 3 presents snapshots that reveal the three-dimensional structure of the dislocation network that was generated by the indentation of the Ta (100) surface discussed above; both the structure immediately after indent and after retraction are displayed. Note that the indenter surface does not look hemispherical in the representation of Fig. 3, but rather bulged out. This is due to the fact that the defect analysis performed by DXA cannot resolve the details of the indentation-pit surface because too many crystal defects agglomerate there; this gives the surface a rather complex shape. After retraction,
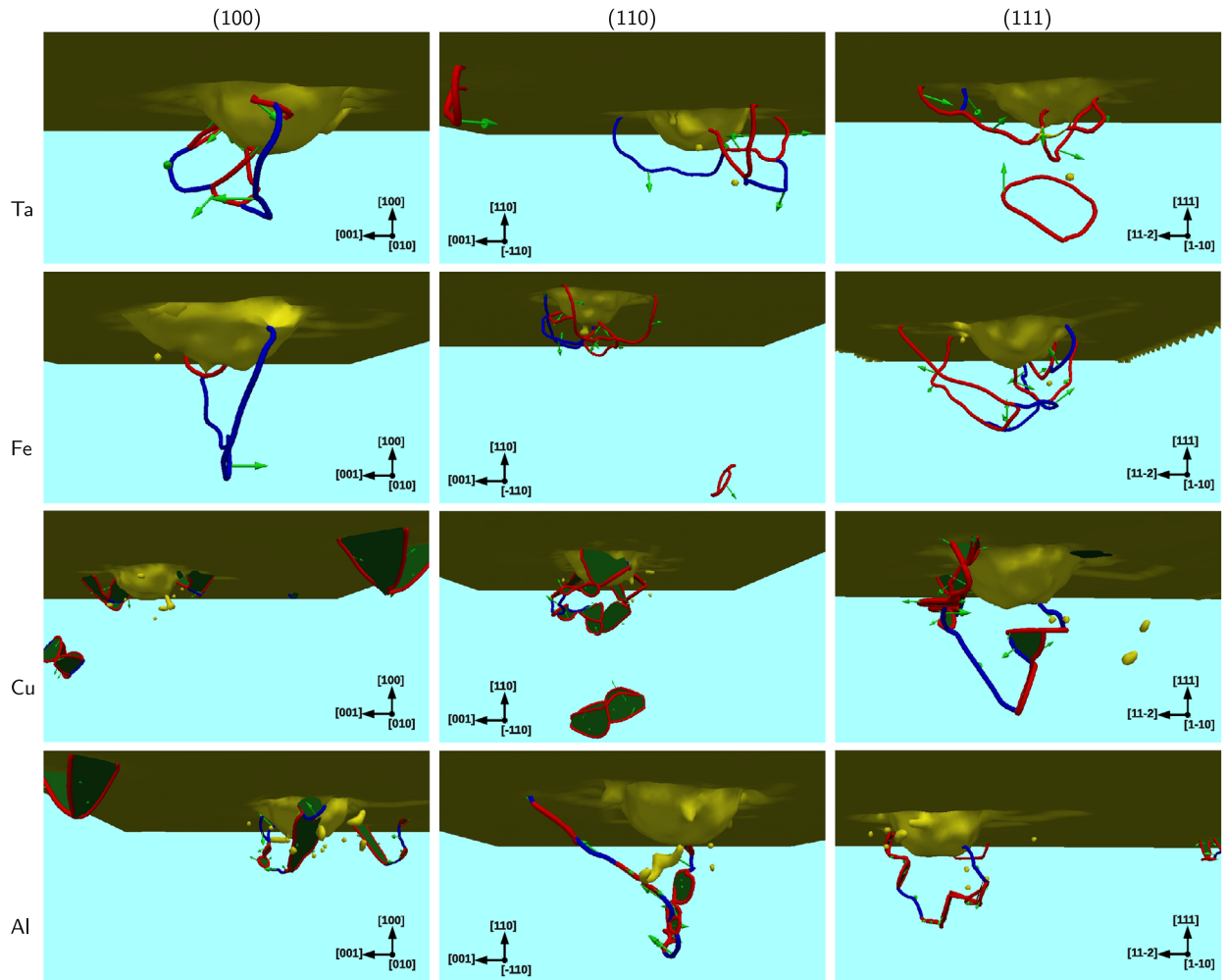
Fig. 5. Synopsis of snapshots showing dislocation network after retraction of the indenter (radius 2.14 nm) into metal surfaces studied at 0 K. The size of the figures varies but can be assessed from the diameter of the indented surface, 4.28 nm. Yellow: deformed surface including unidentified defects. For bcc materials, dislocation lines with Burgers vector $\boldsymbol{b} = \frac{1}{2}\langle 111 \rangle$ are shown in red, those with $\boldsymbol{b} = \langle 100 \rangle$ in blue. For fcc materials, dislocation lines with Burgers vector $\boldsymbol{b} = \frac{1}{6}\langle 112 \rangle$ are shown in red, those with $\boldsymbol{b} = \frac{1}{2}\langle 110 \rangle$ in blue. Green arrows indicate direction of $\boldsymbol{b}$. Dark green areas denote stacking faults. From left to right: (100), (110), (111). First row: Ta. Second row: Fe. Third row: Cu. Fourth row: Al. (For interpretation of the references to color in this figure caption, the reader is referred to the web version of this article.)

however, the indenter imprint has assumed quite well its expected hemispherical form; this again demonstrates that the relaxation induced by the retraction of the indenter is an important aspect for characterizing the defects formed in the plastic zone.

In the case of a bcc substrate such as Ta we observe the generation of dislocations with two different kinds of Burgers vector, $\boldsymbol{b} = \frac{1}{2}\langle 111 \rangle$ and $\boldsymbol{b} = \langle 100 \rangle$; these dislocations are plotted distinctly in Fig. 3. Note that even though dislocations with the first Burgers vector have lower energy, it is known that also dislocations with the larger Burgers vector, $\boldsymbol{b} = \langle 100 \rangle$, may form during indentation by the interaction between dislocations with Burgers vector $\boldsymbol{b} = \frac{1}{2}\langle 111 \rangle$ (Terentyev et al., 2010; Kelly and Knowles, 2012; Gao et al., 2014).

Comparing the dislocation network after indent and after retraction, the general impression is that the network has simplified and its size has shrunk. Indeed, only 9 of the 12 dislocations generated by indentation survive after retraction. However, dislocation reactions have occurred and junctions have formed, in particular between those with $\boldsymbol{b} = \frac{1}{2}\langle 111 \rangle$ and with $\boldsymbol{b} = \langle 100 \rangle$. The network topology has changed quite considerably.

We conclude that the retraction of the indenter relaxes the plastic zone and induces a re-organization of the dislocation network. We shall therefore concentrate in the following discussion on the structure of the network after retraction. We note that in previous experimental work, Bahr et al. (1998) discussed the possibility that dislocations generated during indentation might retreat during unloading and suggested that the mechanism is akin to dislocation damping. More

Table 1
Characteristics of the plastic zone after indent and after retraction of the $R=2.14$ nm indenter at 0 K. Data for 4 metals and 3 orientations each. R_{pl}: radius of plastic zone, f: plastic-zone size factor, L_{disl}: total dislocation length within plastic zone, $\bar{\rho}$: average dislocation density.

Crystal		After indent				After retraction			
		R_{pl} (Å)	f	L_{disl} (Å)	$\bar{\rho}$ (10^{17} m^{-2})	R_{pl} (Å)	f	L_{disl} (Å)	$\bar{\rho}$ (10^{17} m^{-2})
Ta	(100)	58.6	2.7	351.2	0.88	49.0	2.3	270.1	1.20
	(110)	94.3	4.4	797.8	0.46	54.0	2.5	292.6	0.95
	(111)	96.8	4.5	451.0	0.24	60.7	2.8	191.3	0.43
Fe	(100)	60.3	2.8	601.2	1.37	58.9	2.8	199.6	0.49
	(110)	89.7	4.2	763.4	0.51	44.8	2.1	424.0	2.53
	(111)	76.7	3.6	739.9	0.80	59.5	2.8	525.0	1.25
Cu	(100)	84.3	3.9	1666.5	1.35	54.9	2.6	294.9	0.91
	(110)	78.6	3.7	2184.3	2.19	58.8	2.7	728.0	1.78
	(111)	85.8	4.0	1809.2	1.39	59.2	2.8	506.3	1.22
Al	(100)	74.2	3.5	1394.6	1.67	48.4	2.3	263.2	1.21
	(110)	91.1	4.3	1089.1	0.70	64.8	3.0	331.6	0.60
	(111)	69.4	3.2	710.8	1.05	63.2	3.0	330.2	0.65

recently, Montagne et al. (2009), in an experimental study of indentation into MgO, provided an analysis supporting the assumption of dislocation annihilation during unloading.

As described in Section 2.2 our data allow us to define the extent of the plastic zone. The radius of the plastic zone, R_{pl}, is defined as the maximum distance of a dislocation line from the center of the indenter; it amounts to 58.6 Å after indent and 49.0 Å after retraction. The corresponding size factors, $f = R_{pl}/a_c$, amount to 2.7 and 2.3, respectively. These numbers quantify the shrinkage of the plastic zone after retraction; they will be discussed in more detail in connection with the other crystals studied in the Section 3.2.

Up to now, the discussion of indentation into Ta (100) has been focused on the small indenter, $R=2.14$ nm. Fig. 4 shows the dislocation network generated after indent with the large indenter, $R=10$ nm. Here, a different coloring has been applied that emphasizes the extent of the plastic zone. In agreement with the larger contact radius, $a_c=89.6$ Å, the plastic zone extends further than for the small indenter, viz. to 306 Å after indent and to 195 Å after retraction.

Fig. 4 shows a novel feature not visible in Fig. 3: besides dislocations still adherent to the indented surface, also dislocation loops are visible that have become detached from it and move away into the substrate interior. As discussed in Section 2.2, we do not count these dislocations to belong to the plastic zone. Actually, since our crystallites are initially defect-free their motion is mainly limited by the size of the simulation box, in particular if they move along the surface. Not surprisingly the dislocation network looks considerably more complex than for the small indenter. Upon retraction, it shrinks again; several point defects (vacancies) are left behind, which have been created by dislocation reactions. Some of the freely moving dislocation loops have moved inwards towards the indentation tip due to the decrease in the stress field after retraction.

3.2. Dependence on crystal structure and orientation

Similar to the indentation into the Ta (100) surface we performed indentation simulations into the Ta (110) and (111) surfaces, as well as into the three low-indexed surfaces of Fe, Cu and Al. The snapshots in Fig. 5 assemble the dislocation structures after retraction, and Table 1 summarizes the quantitative data characterizing the extent of the plastic zone.

The snapshots, Fig. 5, show a wide variety of dislocation patterns. Typical features are the dichotomy of dislocations still adherent to the indent surface as opposed to emitted dislocation loops. These prismatic loops are emitted in the direction of their Burgers vectors; compare for instance the loop emitted for Ta (110) emitted parallel to the surface and the loop emitted in Ta (111) obliquely downward in $\langle 111 \rangle$ direction. Analogously, in fcc materials, for (100) surfaces – but also for the Al (111) surface – the loops easily glide along the surface, while in Cu (110) a loop is emitted perpendicularly down into the material.

For bcc material the general mix of $\boldsymbol{b} = \frac{1}{2}\langle 111 \rangle$ and $\boldsymbol{b} = \langle 100 \rangle$ dislocations is characteristic. Dislocation reactions leading to triple junctions are typical and lead to the build-up of a complex network structure. Dislocations in fcc materials are typically split into $\boldsymbol{b} = \frac{1}{6}\langle 112 \rangle$ partials separated by a stacking fault; this gives the resulting structure an even more complex shape. However, due to the high shear rates accompanying dislocation nucleation in our simulations here also un-dissociated dislocations with Burgers vector $\boldsymbol{b} = \frac{1}{2}\langle 110 \rangle$ show up, albeit more rarely. For all materials, point defects remaining in the vicinity of the indented surface as the product of dislocation reactions are visible.

Table 1 summarizes our results on the size of the plastic zone. Immediately after indentation, the radius of the plastic zone, R_{pl}, shows a rather large scatter; in units of the contact radius, Eq. (2), these sizes reach values of $f=2.7$–4.4. Note that in the determination of the plastic zone, only the dislocations still adherent to the indentation pit – but not the detached dislocation loops – have been considered. After retraction the size considerably shrinks and in most cases assumes values between $f=2.1$ and 3.0. This result is in agreement with the findings of Durst et al. (2005) that f is in the range of $0 - 3.5$, but narrows down the range of f. We note that for the Cu (100) surface, the results reported have been obtained for a reduced

retraction velocity of 20 m/s. Our standard value of 100 m/s led to an anomalous behavior for this surface, since the plastic zone acquired a radius of 0, and thus also $f=0$. All dislocations adherent to the indenter surface disappeared by annihilation reactions or converted to loops emitted along the surface or into the substrate interior. We avoided this irregular behavior by choosing a smaller retraction speed in this case, thus allowing dislocations to move more gently.

Our data do not allow to extract any systematic differences between fcc and bcc materials, or between the different surface orientations. This applies in particular for the plastic zone after retraction.

The total length of dislocations calculated by DXA can be used to estimate the average dislocation density in the plastic zone using Eq. (3). The dislocation length can be compared to the geometrical estimate of Swadener et al. (2002), Eq. (6). It depends on the size of the Burgers vector b; for our systems b varies only between $b=2.47$ Å for Fe and 2.86 Å for Al and Ta ($b=2.56$ Å for Cu). Swadener's dislocation length thus assumes values between $L_{\text{disl}} = 388$ Å for Fe and 335 Å for Al and Ta (374 Å for Cu).

Comparison with the simulation results of Table 1 shows that the estimate is in the correct order of magnitude, but differs in detail. Immediately after indent, the dislocation length is considerably larger, but reduces after retraction. This is understandable as the stress release after retraction allows the crystal to lower its potential energy by annihilating defects.

Often – but not in all cases – the dislocation length is larger than the geometrical estimate; this is understandable from crystallographic considerations. Swadener et al. assume the prismatic loops generated during indentation all to be oriented with their Burgers vector pointing down into the crystal; this is obviously only true for specific favorable crystal orientations. In the general case, dislocations will be generated with their Burgers vector oriented according to crystallography, see Fig. 5 above. As discussed in Section 1, this argument has been quantified by introducing the Nye factor (Arsenlis and Parks, 1999). Sometimes the resulting dislocation length is below the geometrical estimate. Since dislocation reactions tend to decrease the length of the network, we assume that such reactions are responsible for shorter dislocation lengths. In summary, we conclude that while the geometrical estimate, Eq. (6), provides us with the correct order of magnitude of the dislocation length generated, individual cases may strongly deviate from it.

It appears, however, that fcc crystals produce larger dislocation networks than bcc crystals, in particular immediately after indent. We presume that this fact is connected to the Peierls barrier which assumes systematically lower values in fcc than in bcc materials. The Peierls barrier is defined as the stress necessary to make a dislocation move in a perfect crystal; its magnitude can be estimated from (Nabarro, 1967)

$$\tau_P = \frac{2G}{1-\nu}\exp\left(-\frac{2\pi w}{b}\right),$$

(10)

where G is the shear modulus, ν the Poisson ratio, w is the width of the dislocation core, and b is the length of the Burgers vector. The Peierls barrier thus essentially depends on the width of the dislocation. Since dislocations in fcc crystals are dissociated, they systematically have a large width and a correspondingly small Peierls barrier; values for Cu amount to $\tau_P < 7 \times 10^{-6}$ G and for Al $\tau_P < 56 \times 10^{-6}$ G (Kamimura et al., 2013). The barriers in bcc metals are systematically higher; thus it is $\tau_P = 5.2 \times 10^{-3}$ G for both Fe and Ta (Kamimura et al., 2013).

The average dislocation densities, $\bar{\rho}$, in the plastic zone have been evaluated using Eq. (3). Table 1 shows that they are in the range of 10^{17} m^{-2} both immediately after indent and after retraction. The densities after indent may increase or decrease during retraction; here no systematics is visible: while L_{disl} always shrinks during retraction, so does the size of the plastic zone, and since the density is the ratio of these two quantities, its change is hard to predict. $\bar{\rho}$ shows no systematic dependence on surface orientation or substrate crystal structure.

Our data also allow us to display local dislocation density as a function of the distance to the center of the spherical indenter, see Section 2.2. The resulting densities after retraction are displayed in Fig. 6. We see a simple, mostly unimodal, shape of these densities; they have a maximum at some distance to the indented surface and decay both towards the surface and to the target interior. There is a simple physical reason why the maximum of the dislocation density is at some distance below the surface: dislocation nucleation occurs where shear stresses are maximum; for the stress field exerted by a spherical indenter this occurs at some distance below the surface, at $\sim 0.5a_c$ (the exact position depends slightly on the substrate Poisson ratio) (Johnson, 1985; Fischer-Cripps, 2004). In all cases, the dislocation density decreases towards the target interior as we move away from the place where dislocations are produced. In the majority of the curves in Fig. 6 the dislocation density also decreases towards the surface; this appears natural since the surface provides a sink for dislocations. In some cases displayed in Fig. 6 the dislocation density increases again towards the surface; we have to note, however, that the determination of the exact dislocation density close to the surface is a non-trivial task for the DXA (or any other) dislocation detection algorithm.

It is nowadays possible to detect the dislocation density produced by nanoindentation experimentally in their 3D structure (Zaefferer et al., 2008; Demir et al., 2009; Pharr et al., 2010); previously transmission electron microscopy could be used to obtain 2D top views of the generated dislocations (Chiu and Ngan, 2002). The novel technique uses electron backscatter diffraction on serial sections of the indented material, thus providing a three-dimensional image of the indentation-induced lattice rotations in the indented zone. From these data the authors could calculate the induced dislocation densities for Cu single crystals. These densities show qualitatively the same features as those shown in Fig. 6: the maximum density is close to the indenter surface and decreases towards the target inner. In the cases studied (indentation to around 1 μm) the plastic zone extended to roughly $2a_c$ where the dislocation density decreased by 2 orders of magnitude
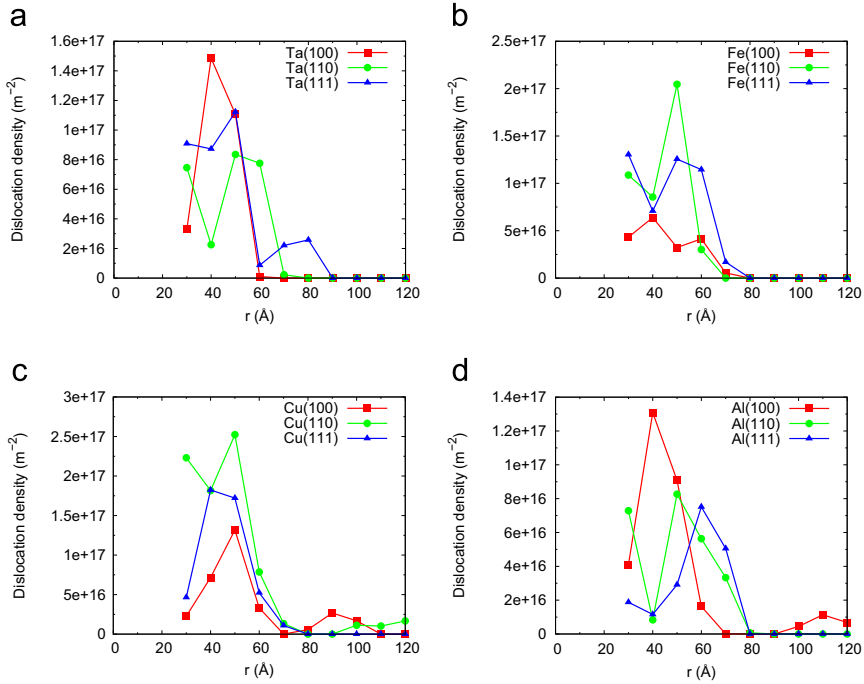
Fig. 6. Local dislocation density after retraction of the indenter (radius 2.14 nm) at 0 K for all crystals. a: Ta, b: Fe, c: Cu, d: Al.

from the values at the indented surface. These studies also showed – for the example of indents into the Cu (111) surface – that the pile-up patterns on the surface are directly correlated with an increased dislocation density underneath (Zaafarani et al., 2006, 2008). In addition, these studies find that the initially single-crystalline substrate material underwent a complicated pattern of crystal rotations and counter-rotations (Zaafarani et al., 2006). It is caused by the fact that depending on the location with respect to the indenter different slip systems are activated locally leading to different local lattice rotations. Zaafarani et al. (2008) showed that crystal plasticity theory is necessary for successfully modeling the lattice rotations. Begau et al. (2012) provide a recent overview on this phenomenon and show how to determine lattice rotations from atomistic simulation.

3.3. Size dependence

We study the effect of the indenter size for the case of the Ta substrate. Here our relatively large sample dimensions, cf. Section 2.1, allow us to perform indentations with an indenter of radius $R = 10$ nm. The resulting dislocation network structures after retraction are presented in Fig. 7, and the quantitative characteristics of the plastic zone are assembled in Table 2.

The geometrical estimate, Eq. (6), predicts a value of $L_{disl} = 5268$ Å. The results after indentation are a factor of 2.3–2.5 larger. This finding is similar to what we discussed above for the small indenter; in addition to geometrically necessary dislocations, also statistical dislocations have been produced. Note that the dislocation length is here quite independent of the surface orientation; the larger indentation depth and the resulting plastic zone appear to smoothen out the influence of
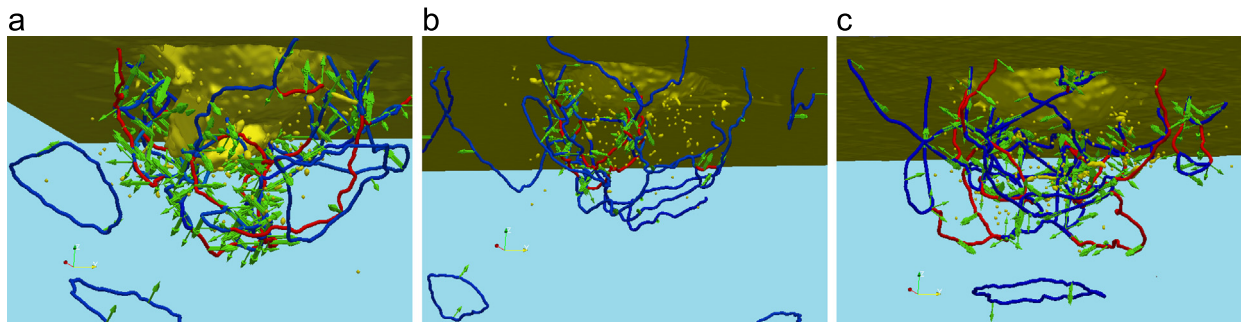

Fig. 7. Snapshots showing defects and dislocation network after retraction of the indenter (radius 10 nm) into Ta surfaces at 300 K. Colors as in Fig. 3. The diameter of the indented surface amounts to $2a_c = 179.2$ Å. a: (100). b: (110). c: (111).

Table 2
Characteristics of the plastic zone after indent and after retraction of the $R=10$ nm indenter in Ta at 300 K. Notation as in Table 1.

Crystal	After indent				After retraction			
	R_{pl} (Å)	f	L_{disl} (Å)	$\bar{\rho}$ (10^{16} m^{-2})	R_{pl} (Å)	f	L_{disl} (Å)	$\bar{\rho}$ (10^{16} m^{-2})
(100)	306	3.4	12349	2.2	195	2.3	6787	4.7
(110)	342	3.8	13452	1.6	176	2.2	1840	1.5
(111)	324	3.6	13480	2.5	202	2.5	1036	6.2

the surface orientation to some degree. Upon retraction, the length of the dislocations strongly shrinks, in particular for the (110) and (111) surfaces.

According to Eq. (7), the dislocation density should simply scale with $1/R$, independently of the indentation depth and the contact radius, as long as the plastic zone size factor, f, does not change. For equal f values, the density produced by the large indenter should be a factor of 5 smaller than that produced by the small indenter. Comparing the data of Tables 1 and 2, we see that the dislocation densities for the two indents are of quite comparable magnitude; the dislocation density produced by the small indenter varies between a factor of 6 and 0.7 relative to that produced by the large indenter. This comparison demonstrates that it is in particular the size of the plastic zone, f, that determines the average dislocation density, since it enters Eq. (7) with the third power.

The results on the size of the plastic zone are in close agreement to our findings for the small indenter, Table 1. The rather high value of $f=3.4$–3.8 immediately after indentation is strongly reduced by retraction. The resulting values of $f=2.2$–2.5 are in satisfactory agreement with our results for the small indenter, $f=2.3$–2.8, Table 1.

Fig. 8 displays the local dislocation densities. Due to the larger size of the plastic zone, the plots show a smaller statistical error than for the small indenter, Fig. 6. Note that the dislocation density does not vanish outside of the plastic zone, since the density of dislocation loops emitted from the plastic zone is included in this plot, Fig. 8. The spatial structure looks rather similar for all 3 surfaces investigated.

For the indents with the large indenter, we also study the topography of the imprint and the pile-up in the way an AFM apparatus (with a sharp tip) would monitor it and display it in Fig. 9. The simulated pile-ups look similar to the ones obtained previously for a smaller indenter ($D=8$ nm diameter) (Ruestes et al., 2014). This figure allows us to discuss the slip systems active in these indents. For the 3 surface orientations we observe the following features of the crystallography of the slips:

- (100): For the indentation of a (100) plane, slip occurs along $\langle 111 \rangle$ slip directions. They make an angle of 35° to the surface and have a $\langle 110 \rangle$ component when projected onto the (100) surface. Then as a consequence of the four $\langle 111 \rangle$ directions present together with the crystallographic symmetry of the (100) plane, a four-fold symmetry arises. In this case the slip extends 14.1 nm on the surface.
- (110): Four slip directions lie in the surface plane. The two downward directed slip vectors $[\bar{1}\bar{1}1]$ and $[\bar{1}\bar{1}\bar{1}]$ have projections $[001]$ and $[00\bar{1}]$ into the surface plane. Their angle to the surface is 54°. The intersection angle is not 90° as in the (100) case, therefore leading to a two-fold symmetry. Here the slip extends only 9–10 nm on the surface; this small distance is due to the high angle of the slip to the surface.
- (111): Four slip directions are activated, namely $[1\bar{1}1]$, $[\bar{1}11]$, $[11\bar{1}]$ and $[\bar{1}\bar{1}\bar{1}]$. The projections of the first three directions onto the (111) surface plane amount to $[11\bar{2}]$, $[1\bar{2}1]$, and $[\bar{2}11]$; these are responsible for the three-fold symmetry of the
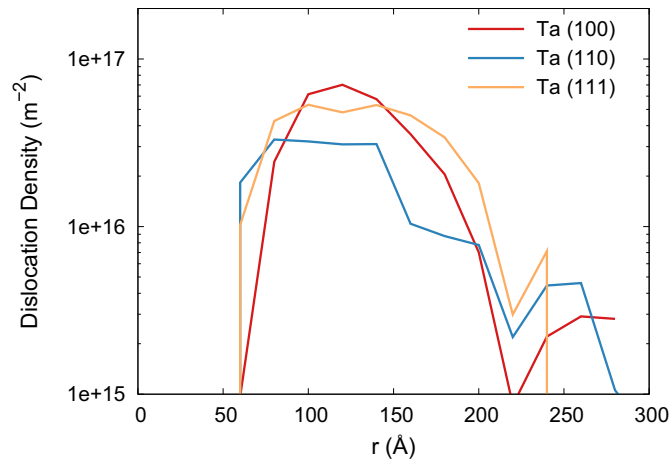

Fig. 8. Local dislocation density after retraction of the indenter (radius 10 nm) for Ta crystals at 300 K.
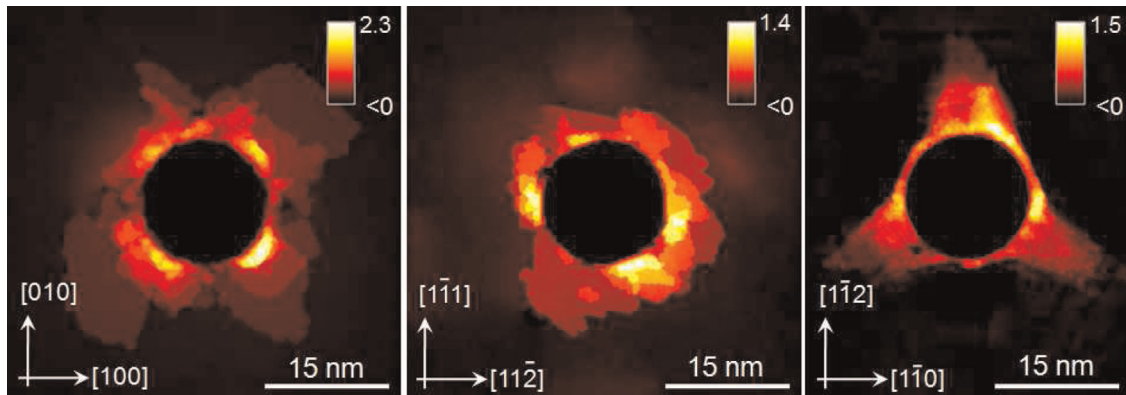
Fig. 9. Top view of the indentation imprints in Ta surfaces after retraction of the indenter (radius 10 nm) at 300 K. From left to right: (100), (110), (111). Color-scale indicates pile-up height in nm. (For interpretation of the references to color in this figure caption, the reader is referred to the web version of this article.)

produced slip pattern on the (111) surface. The corresponding slip vectors make an angle of only $19.5°$ to the surface, causing the slip to extend far on the surface, between 14.3 to 14.8 nm. The fourth slip vector, $[\bar{1}\bar{1}\bar{1}]$, goes perpendicular down into the target and thus has no trace on the surface.

The pile-up pattern shown here is characteristic of the crystal orientation that was indented. To our knowledge, Smith et al. (2003) were the first to provide such patterns using MD; the pile-ups of (100) and (111) Fe surfaces indented with a pyramidal indenter were in good qualitative agreement with corresponding experimental results. In later work, Wang et al. (2004) used crystal plasticity continuum modeling to calculate pile-up patterns in Cu single crystals and obtained good agreement with corresponding experiments. For the example of the Cu (111) surface, the pile-up patterns on the surface could be shown to be directly correlated with an increased density of mobile dislocations underneath (Zaafarani et al., 2006, 2008).

4. Conclusions

Using classical molecular-dynamics simulation we study nanoindentation of bcc and fcc single crystals by a spherical indenter. The effect of crystal structure, surface orientation, indenter radius, penetration depth, penetration rate and temperature is inspected to determine their influence on the extent of the plastic zone and the length of the dislocations produced.

1. The dislocation structure shows that the generated dislocations always fall into two different dislocation groups: those that adhere to the indentation pit, and those that have been emitted. The latter group consists of prismatic dislocation loops ejected into the substrate interior or gliding along the surface. We use the first group to define the extent of the plastic zone.
2. Immediately after indentation the plastic zones are more extended than after indenter retraction; this is a consequence of relaxation processes occurring in the material after unloading.
3. The plastic-zone size factor f – defined as the ratio of the radius of the plastic zone to the contact radius, Eq. (2) – assumes (after retraction) values between 2 and 3. It does not systematically depend on crystal structure (fcc or bcc), surface orientation, indenter size or penetration depth. Immediately after indentation f is substantially larger, between 3 and 4.
4. The generated dislocation network looks far more complicated than the simple idea of a sequence of prismatic dislocation loops that has been used in geometrical estimates of the length of the dislocations produced (Nix and Gao, 1998; Swadener et al., 2002). This is the consequence of two effects: (i) the crystal orientation usually does not allow slip perpendicular to the surface; (ii) dislocation reactions in the high-density plastic zone interconnect the network of generated dislocations.
5. Nevertheless, the geometrical estimate of the dislocation length presented by Swadener et al. (2002) gives a fair presentation of the order of magnitude; individual results, however, differ. Dislocation reactions shorten the network, while crystallographic aspects – such as the orientation of slip planes and directions with respect to the surface – may lengthen it.
6. Immediately after indentation, the dislocation network in fcc crystals is more extended than in bcc crystals; we ascribe this to the considerably lower Peierls barrier in fcc crystals. After retraction, this difference is no longer visible.
7. The radial distribution of dislocations shows a simple unimodal structure with a maximum at roughly twice the contact radius below the initial surface. It decays towards the surface and towards the target inner, since these regions constitute sinks for dislocations.

Acknowledgments

Appendix A. Sensitivity

When using molecular dynamics simulation to study the indentation process, the indentation speed (some m/s) is considerably higher than in experiment (some μm/s). The high speed used in simulation is dictated by the computational resources, and it appears unfeasible nowadays to simulate nanoindentation using the experimental speed. We shall explore in Section A.1 – within the limits of what is computationally feasible – the effect of the indentation speed on the plastic zone.

While experiments are usually performed at room temperature, simulations of defect structures are often done at low temperatures to ease defect identification. We explore the influence of the substrate temperature in Section A.2.

A.1. Indentation velocity

The influence of the indentation speed – varied between $v = 10$ and 100 m/s – on the characteristics of the plastic zone is presented in Table 3. Evidently a speed of 100 m/s suppresses dislocation nucleation almost entirely, and thus constitutes a too high velocity to use in simulations. In the range of 10–50 m/s, the size of the plastic zone shows little variation, but the length of the dislocations shows a maximum for 20 m/s. We checked whether another plasticity mechanism plays a role in this case, and looked for twin formation using the CAT software; however, no twins could be identified. We conclude that variations in indentation velocity may change the amount of plasticity formed by as much as 40%; however, the size of the plastic zone is quite stable.

We note that similar tests of the influence of the indentation speed (34 m/s and 10 m/s) for indentation with the big indenter into the Ta target gave no significant differences. Alcalá et al. (2012) performed MD simulations of Ta nanoindentation for velocities of 4–0.004 m/s; they report that the plasticity mechanisms showed no significant differences in this velocity range. They also point out that the larger indentation velocities (around 4 m/s) are more appropriate for modeling experiments, since these are usually conducted at constant load – in contrast to constant displacement in the simulation. We conclude that the indentation speeds used in our simulations are in the range of those commonly used in nanoindentation simulations (Lodes et al., 2011).

A.2. Temperature

Data of the temperature dependence of the size and the dislocation length are presented in Table 4. The data show changes on the 20% level in the length of the dislocation network with temperature increase; these appear to represent fluctuations rather than a trend. Changes in the size of the plastic zone are small.

Table 3
Influence of indentation velocity v on the characteristics of the dislocation network. Data taken after full indentation of the $R = 2.14$ nm indenter into the Fe (100) surface at $T = 0$ K. Notation as in Table 1.

v (m/s)	R_{pl} (Å)	f	L_{disl} (Å)	$\bar{\rho}$ (10^{17} m^{-2})
10	52.9	2.5	369.1	1.28
20	60.3	2.8	601.2	1.37
50	59.1	2.8	476.1	1.16
100	51.5	2.4	55.2	0.21

Table 4
Influence of temperature T on the characteristics of the dislocation network. Data taken after retraction of the $R = 10$ nm indenter into the Ta (100) surface with velocity $v = 34$ m/s. Notation as in Table 1.

T (K)	R_{pl} (Å)	f	L_{disl} (Å)	$\bar{\rho}$ (10^{16} m^{-2})
10	195	2.3	6787	4.7
300	203	2.4	6516	3.9

Lee et al. (2013) investigate temperature effects in indentation by performing indentation experiments at temperatures between 160 K and room temperature for several single crystalline materials: Nb, W, Al, and Au. They find a strong influence of temperature for the three first metals, but not for Au; this temperature dependence is attributed to the probability of dislocation cross-slip and its temperature dependence. We note that in MD simulations thermally activated processes are unlikely to happen due to the high indentation velocity, and hence the effect of temperature is small. Indeed, Alcalá et al. (2012) performed MD simulations of Ta nanoindentation for temperatures in the range of 77–900 K. They report systematic changes in the defect nucleation stage; the load drops associated with defect nucleation occur at smaller pressures and decrease in height with increasing temperature. They did not report, however, on the size of the plastic zone or the density of the dislocation network. We conclude that the influence of temperature in the range below 300 K on the plastic zone in atomistic simulation can be assumed to be minor.

References

Abbaschian, R., Abbaschian, L., Reed-Hill, R.E., 2010. Physical Metallurgy Principles, 4th edition Cengage Learning, Stamford, CT.

Al-Rub, R.K.A., Voyiadjis, G.Z., 2004. Analytical and experimental determination of the material intrinsic length scale of strain gradient plasticity theory from micro- and nano-indentation experiments. Int. J. Plast. 20 (6), 1139–1182. doi: http://dx.doi.org/10.1016/j.ijplas.2003.10.007.

Alcalá, J., Dalmau, R., Franke, O., Biener, M., Biener, J., Hodge, A., 2012. Planar defect nucleation and annihilation mechanisms in nanocontact plasticity of metal surfaces. Phys. Rev. Lett. 109, 075502.

Arsenlis, A., Parks, D.M., 1999. Crystallographic aspects of geometrically-necessary and statistically-stored dislocation density. Acta Mater. 47, 1597.

Asenjo, A., Jaafar, M., Carrasco, E., Rojo, J.M., 2006. Dislocation mechanisms in the first stage of plasticity of nanoindented Au (111) surfaces. Phys. Rev. B 73, 075431.

Bahr, D.F., Kramer, D.E., Gerberich, W.W., 1998. Non-linear deformation mechanisms during nanoindentation. Acta Mater. 46, 3605.

Banerjee, S., Naha, S., Puri, I.K., 2008. Molecular simulation of the carbon nanotube growth mode during catalytic synthesis. Appl. Phys. Lett. 92, 233121.

Begau, C., Hua, J., Hartmaier, A., 2012. A novel approach to study dislocation density tensors and lattice rotation patterns in atomistic simulations. J. Mech. Phys. Solids 60 (4), 711–722. doi: http://dx.doi.org/10.1016/j.jmps.2011.12.005.

Biener, M.M., Biener, J., Hodge, A.M., Hamza, A.V., 2007. Dislocation nucleation in bcc ta single crystals studied by nanoindentation. Phys. Rev. B 76, 165422.

Cao, Y., Xue, Z., Chen, X., Raabe, D., 2008. Correlation between the flow stress and the nominal indentation hardness of soft metals. Scr. Mater. 59, 518.

Carrasco, E., Rodríguez de la Fuente, O., Rojo, J.M., 2008. Dislocation emission at the onset of plasticity during nanoindentation in gold. Philos. Mag. 88, 281.

Chicot, D., 2009. Hardness length-scale factor to model nano- and micro-indentation size effects. Mater. Sci. Eng. A 499, 454.

Chiu, Y.L., Ngan, A.H.W., 2002. A TEM investigation on indentation plastic zones in Ni$_3$Al (Cr, B) single crystals. Acta Mater. 50, 2677.

Christopher, D., Smith, R., Richter, A., 2001. Atomistic modelling of nanoindentation in Fe and Ag. Nanotechnology 12, 372.

Cordill, M.J., Lund, M.S., Parker, J., Leighton, C., Nair, A.K., Farkas, D., Moody, N.R., Gerberich, W.W., 2009. The nano-Jackhammer effect in probing near-surface mechanical properties. Int. J. Plast. 25 (11), 2045–2058. doi: http://dx.doi.org/10.1016/j.ijplas.2008.12.015.

Dai, X.D., Kong, Y., Li, J.H., Liu, B.X., 2006. Extended Finnis–Sinclair potential for bcc and fcc metals and alloys. J. Phys.: Condens. Matter 18, 4527.

Demir, E., Raabe, D., Zaafarani, N., Zaefferer, S., 2009. Investigation of the indentation size effect through the measurement of the geometrically necessary dislocations beneath small indents of different depths using EBSD tomography. Acta Mater. 57, 559.

Durst, K., Backes, B., Göken, M., 2005. Indentation size effect in metallic materials: correcting for the size of the plastic zone. Scr. Mater. 52, 1093.

Engels, P., Ma, A., Hartmaier, A., 2012. Continuum simulation of the evolution of dislocation densities during nanoindentation. Int. J. Plast. 38 (0), 159–169. doi: http://dx.doi.org/10.1016/j.ijplas.2012.05.010.

Faghihi, D., Voyiadjis, G.Z., 2012. Determination of nanoindentation size effects and variable material intrinsic length scale for body-centered cubic metals. Mech. Mater. 44 (0), 189–211. doi: http://dx.doi.org/10.1016/j.mechmat.2011.07.002.

Faken, D., Jonsson, H., 1994. Systematic analysis of local atomic structure combined with 3D computer graphics. Comput. Mater. Sci. 2, 279.

Fischer-Cripps, A.C., 2004. Nanoindentation, 2nd edition Springer, New York.

Gao, H., Huang, Y., Nix, W.D., Hutchinson, J.W., 1999. Mechanism-based strain gradient plasticity. I. Theory. J. Mech. Phys. Solids 47 (6), 1239–1263. doi: http://dx.doi.org/10.1016/S0022-5096(98)00103-3.

Gao, Y., Ruestes, C.J., Urbassek, H.M., 2014. Nanoindentation and nanoscratching of iron: atomistic simulation of dislocation generation and reactions. Comput. Mater. Sci. 90, 232–240.

Gerberich, W.W., Tymiak, N.I., Grunlan, J.C., Horstemeyer, M.F., Baskes, M.I., 2002. Interpretations of indentation size effects. J. Appl. Mech. 69, 433.

Gouldstone, A., Chollacoop, N., Dao, M., Li, J., Minor, A.M., Shen, Y.-L., 2007. Indentation across size scales and disciplines: recent developments in experimentation and modeling. Acta Mater. 55, 4015.

Graca, S., Colaco, R., Carvalho, P.A., Vilar, R., 2008. Determination of dislocation density from hardness measurements in metals. Mater. Lett. 62, 3812.

Gunkelmann, N., Bringa, E.M., Kang, K., Ackland, G.J., Ruestes, C.J., Urbassek, H.M., 2012. Polycrystalline iron under compression: plasticity and phase transitions. Phys. Rev. B 86, 144111.

Hagelaar, J.H.A., Bitzek, E., Flipse, C.F.J., Gumbsch, P., 2006. Atomistic simulations of the formation and destruction of nanoindentation contacts in tungsten. Phys. Rev. B 73, 045425.

Harrison, R.J., Voter, A.F., Chen, S.-P., 1989. An embedded atom potential for bcc iron. In: Vitek, V., Srolovitz, D.J. (Eds.), Atomistic Simulation of Materials. Plenum Press, New York, pp. 219.

Henderson, A., 2007. Paraview Guide, A Parallel Visualization Application, Kitware Inc., ⟨http://www.paraview.org⟩.

Hua, J., Hartmaier, A., 2010. Determining Burgers vectors and geometrically necessary dislocation densities from atomistic data. Model. Simul. Mater. Sci. Eng. 18, 045007.

Huang, Y., Xue, Z., Gao, H., Nix, W.D., Xia, Z.C., 2000. A study of microindentation hardness tests by mechanism-based strain gradient plasticity. J. Mater. Res. 15, 1786.

Huang, Y., Feng, X., Pharr, G.M., Hwang, K.C., 2007. A nano-indentation model for spherical indenters. Model. Simul. Mater. Sci. Eng. 15 (1), S255.

Hull, D., Bacon, D.J., 1984. Introduction to Dislocations, 3rd edition Pergamon, Oxford.

Johnson, K.L., 1985. Contact Mechanics. Cambridge University Press, Cambridge.

Ju, S.-P., Wang, C.-T., Chien, C.-H., Huang, J.C., Jian, S.-R., 2007. The nanoindentation responses of nickel surfaces with different crystal orientations. Mol. Simul. 33, 905.

Kamimura, Y., Edagawa, K., Takeuchi, S., 2013. Experimental evaluation of the Peierls stresses in a variety of crystals and their relation to the crystal structure. Acta Mater. 61 (1), 294–309. doi: http://dx.doi.org/10.1016/j.actamat.2012.09.059.

Kelchner, C.L., Plimpton, S.J., Hamilton, J.C., 1998. Dislocation nucleation and defect structure during surface indentation. Phys. Rev. B 58, 11085.

Kelly, A., Knowles, K.M., 2012. Crystallography and Crystal Defects, 2nd edition John Wiley, Chichester, UK.

Kiely, J.D., Hwang, R.Q., Houston, J.E., 1998. Effect of surface steps on the plastic threshold in nanoindentation. Phys. Rev. Lett. 81, 4424.

Kim, J.-Y., Lee, B.-W., Read, D.T., Kwon, D., 2005. Influence of tip bluntness on the size-dependent nanoindentation hardness. Scr. Mater. 52 (5), 353–358. doi: http://dx.doi.org/10.1016/j.scriptamat.2004.10.036.

Kumar, N.N., Tewari, R., Durgaprasad, P.V., Dutta, B.K., Dey, G.K., 2013. Active slip systems in bcc iron during nanoindentation: a molecular dynamics study. Comput. Mater. Sci. 77, 260.

Lee, Y., Park, J.Y., Kim, S.Y., Jun, S., Im, S., 2005. Atomistic simulations of incipient plasticity under al(111) nanoindentation. Mech. Mater. 37, 1035.

Lee, T., Baskes, M.I., Valone, S.M., Doll, J.D., 2012. Atomistic modeling of thermodynamic equilibrium and polymorphism of iron. J. Phys.: Condens. Matter 24, 225404.

Lee, S.-W., Meza, L., Greer, J.R., 2013. Cryogenic nanoindentation size effect in [001]-oriented face-centered cubic and body-centered cubic single crystals. Appl. Phys. Lett. 103 (10), 101906. doi: http://dx.doi.org/10.1063/1.4820585.

Li J., Ngan A.H.W. and Gumbsch P., Atomistic modeling of mechanical behavior, Acta Mater. 51 (19), 2003, 5711–5742, doi: http://dx.doi.org/10.1016/j.actamat.2003.08.002.

Li, Y., Siegel, D.J., Adams, J.B., Liu, X.-Y., 2003. Embedded-atom-method tantalum potential developed by the force-matching method. Phys. Rev. B 67, 125101 , http://dx.doi.org/10.1103/PhysRevB.67.125101.

Li, J., 2003. Atomeye: an efficient atomistic configuration viewer. Model. Simul. Mater. Sci. Eng. 11, 173. ⟨http://li.mit.edu/Archive/Graphics/A/⟩.

Liang, H., Woo, C.H., Huang, H., Ngan, A.H.W., Yu, T.X., 2004. Crystalline plasticity on copper (001), (110), and (111) surfaces during nanoindentation. Comput. Model. Eng. Sci. 6, 105.

Lilleodden, E.T., Zimmermann, J.A., Foiles, S.M., Nix, W.D., 2003. Atomistic simulations of elastic deformation and dislocation nucleation during na-noindentation. J. Mech. Phys. Solids 51, 901.

Lodes, M.A., Hartmaier, A., Göken, M., Durst, K., 2011. Influence of dislocation density on the pop-in behavior and indentation size effect in CaF_2 single crystals: experiments and molecular dynamics simulations. Acta Mater. 59, 4264.

Lu, C., Gao, Y., Michal, G., Deng, G., Huynh, N.N., Zhu, H., Liu, X., Tieu, A.K., 2009a. Experiment and molecular dynamics simulation of nanoindentation of body centered cubic iron. J. Nanosci. Nanotechnol. 9, 7307.

Lu, C., Gao, Y., Michal, G., Huynh, N.N., Zhu, H.T., Tieu, A.K., 2009b. Atomistic simulation of nanoindentation of iron with different indenter shapes. Proc. Inst. Mech. Eng. J: J. Eng. Tribol. 223, 977.

Ma, X.-L., Yang, W., 2003. Molecular dynamics simulation on burst and arrest of stacking faults in nanocrystalline Cu under nanoindentation. Nano-technology 14, 1208.

Malerba, L., Marinica, M.C., Anento, N., Bj?rkas, C., Nguyen, H., Domain, C., Djurabekova, F., Olsson, P., Nordlund, K., Serra, A., Terentyev, D., Willaime, F., Becquart, C.S., 2010. Comparison of empirical interatomic potentials for iron applied to radiation damage studies. J. Nucl. Mater. 406, 19.

Mason, J.K., Lund, A.C., Schuh, C.A., 2006. Determining the activation energy and volume for the onset of plasticity during nanoindentation. Phys. Rev. B 73, 054102.

Mendelev, M.I., Han, S., Srolovitz, D.J., Ackland, G.J., Sun, D.Y., Asta, M., 2003. Development of new interatomic potentials appropriate for crystalline and liquid iron. Philos. Mag. 83, 3977.

Mendelev, M., Kramer, M., Becker, C., Asta, M., 2008. Analysis of semi-empirical interatomic potentials appropriate for simulation of crystalline and liquid Al and Cu. Philos. Mag. 88, 1723.

Mishin, Y., Mehl, M.J., Papaconstantopoulos, D.A., Voter, A.F., Kress, J.D., 2001. Structural stability and lattice defects in copper: ab initio, tight-binding, and embedded-atom calculations. Phys. Rev. B 63, 224106.

Montagne, A., Tromas, C., Audurier, V., Woirgard, J., 2009. A new insight on reversible deformation and incipient plasticity during nanoindentation test in MgO. J. Mater. Res. 24, 883.

Muraishi, S., 2013. Triangular dislocation loop model for indented material. Mech. Mater. 56, 106–121. doi: http://dx.doi.org/10.1016/j.mechmat.2012.10.006.

Nabarro, F.R.N., 1967. Theory of Crystal Dislocations. Clarendon Press, Oxford.

Nix, W.D., Gao, H., 1998. Indentation size effects in crystalline materials: a law for strain gradient plasticity. J. Mech. Phys. Solids 46, 411.

Paul, W., Oliver, D., Miyahara, Y., Grütter, P.H., 2013. Minimum threshold for incipient plasticity in the atomic-scale nanoindentation of Au(111). Phys. Rev. Lett. 110, 135506.

Pharr, G.M., Herbert, G., Gao, Y., 2010. The indentation size effect: a critical examination of experimental observations and mechanistic interpretations. Annu. Rev. Mater. Res. 40, 271.

Plimpton, S., 1995. Fast parallel algorithms for short-range molecular dynamics. J. Comput. Phys. 117, 1–19. ⟨http://lammps.sandia.gov/⟩.

Pugno, N.M., 2007. A general shape/size-effect law for nanoindentation. Acta Mater. 55 (6), 1947–1953. doi: http://dx.doi.org/10.1016/j.actamat.2006.10.053.

Qiao, X.G., Starink, M.J., Gao, N., 2010. The influence of indenter tip rounding on the indentation size effect. Acta Mater. 58, 3690.

Qu, S., Huang, Y., Nix, W.D., Jiang, H., Zhang, F., Hwang, K.C., 2004. Indenter tip radius effect on the Nix–Gao relation in micro- and nanoindentation hardness experiments. J. Mater. Res. 19, 3423–3434, http://dx.doi.org/10.1557/JMR.2004.0441.

Qu, S., Huang, Y., Pharr, G.M., Hwang, K.C., 2006. The indentation size effect in the spherical indentation of iridium: a study via the conventional theory of mechanism-based strain gradient plasticity. Int. J. Plast. 22 (7), 1265–1286. doi: http://dx.doi.org/10.1016/j.ijplas.2005.07.008.

Ravelo, R., An, Q., Germann, T.C., Holian, B.L., 2012. Large-scale molecular dynamics simulations of shock induced plasticity in tantalum single crystals. AIP Conf. Proc. 1426, 1263.

Ravelo, R., Germann, T.C., Guerrero, O., An, Q., Holian, B.L., 2013. Shock-induced plasticity in tantalum single crystals: interatomic potentials and large-scale molecular-dynamics simulations. Phys. Rev. B 88, 134101, http://dx.doi.org/10.1103/PhysRevB.88.134101.

Reuber, C., Eisenlohr, P., Roters, F., Raabe, D., 2014. Dislocation density distribution around an indent in single-crystalline nickel: comparing nonlocal crystal plasticity finite-element predictions with experiments. Acta Mater. 71, 333.

Ruestes, C.J., Stukowski, A., Tang, Y., Tramontina, D.R., Erhart, P., Remington, B.A., Urbassek, H.M., Meyers, M.A., Bringa, E.M., 2014. Atomistic simulation of tantalum nanoindentation: effects of indenter diameter, penetration velocity, and interatomic potentials on defect mechanisms and evolution. Mat. Sci. Eng. A 613, 390–403. doi: http://dx.doi.org/10.1016/j.msea.2014.07.001.

Smith, R., Christopher, D., Kenny, S.D., Richter, A., Wolf, B., 2003. Defect generation and pileup of atoms during nanoindentation of Fe single crystals. Phys. Rev. B 67, 245405.

Stukowski, A., Albe, K., 2010. Extracting dislocations and non-dislocation crystal defects from atomistic simulation data. Model. Simul. Mater. Sci. Eng. 18, 085001.

Stukowski, A., Arsenlis, A., 2012. On the elastic–plastic decomposition of crystal deformation at the atomic scale. Model. Simul. Mater. Sci. Eng. 20, 035012.

Stukowski, A., Bulatov, V.V., Arsenlis, A., 2012. Automated identification and indexing of dislocations in crystal interfaces. Model. Simul. Mater. Sci. Eng. 20, 085007.

Stukowski, A., 2010. Visualization and analysis of atomistic simulation data with OVITO – the Open Visualization Tool. Model. Simul. Mater. Sci. Eng. 18, 015012. ⟨http://www.ovito.org/⟩.

Stukowski, A., 2012. Structure identification methods for atomistic simulations of crystalline materials. Model. Simul. Mater. Sci. Eng. 20, 045021.

Swadener, J.G., George, E.P., Pharr, G.M., 2002. The correlation of the indentation size effect measured with indenters of various shapes. J. Mech. Phys. Solids 50, 681.

Tabor, D., 1951. The Hardness of Metals. Clarendon Press, Oxford.

Taylor, G.I., 1934. The mechanism of plastic deformation of crystals. Part I. Theoretical. Proc. Roy. Soc. Lond. Ser 145, 362.

Taylor, G.I., 1934. The mechanism of plastic deformation of crystals. Part II. Comparison with observations. Proc. Roy. Soc. Lond. Ser. A 145, 388.

Terentyev, D.A., Osetsky, Y.N., Bacon, D.J., 2010. Effects of temperature on structure and mobility of the ⟨100⟩ edge dislocation in body-centred cubic iron. Acta Mater. 58, 2477.

Tsuru, T., Shibutani, Y., 2007. Anisotropic effects in elastic and incipient plastic deformation under (001), (110), and (111) nanoindentation of Al and Cu. Phys. Rev. B 75, 035415.

Van Vliet, K.J., Li, J., Zhu, T., Yip, S., Suresh, S., 2003. Quantifying the early stages of plasticity through nanoscale experiments and simulations. Phys. Rev. B 67, 104105.

Voter, A.F., Montalenti, F., Germann, T.C., 2002. Extending the time scale in atomistic simulation of materials. Annu. Rev. Mater. Res. 32, 321.

Wang, Y., Raabe, D., Klber, C., Roters, F., 2004. Orientation dependence of nanoindentation pile-up patterns and of nanoindentation microtextures in copper single crystals. Acta Mater. 52, 2229.

Wo, P.C., Zuo, L., Ngan, A.H.W., 2005. Time-dependent incipient plasticity in Ni$_3$Al as observed in nanoindentation. J. Mater. Res. 20, 489–495, http://dx.doi. org/10.1557/JMR.2005.0056.

Yang, B., Vehoff, H., 2007. Dependence of nanohardness upon indentation size and grain size – a local examination of the interaction between dislocations and grain boundaries. Acta Mater. 55, 849.

Yao, W.Z., Krill III, C.E., Albinski, B., Schneider, H.-C., You, J.H., 2014. Plastic material parameters and plastic anisotropy of tungsten single crystal: a spherical micro-indentation study. J. Mater. Sci. 49, 3705.

Zaafarani, N., Raabe, D., Singh, R.N., Roters, F., Zaefferer, S., 2006. Three-dimensional investigation of the texture and microstructure below a nanoindent in a cu single crystal using 3D EBSD and crystal plasticity finite element simulations. Acta Mater. 54, 1863.

Zaafarani, N., Raabe, D., Roters, F., Zaefferer, S., 2008. On the origin of deformation-induced rotation patterns below nanoindents. Acta Mater. 56, 31.

Zaefferer, S., Wright, S.I., Raabe, D., 2008. Three-dimensional orientation microscopy in a focused ion beam-scanning electron microscope: a new dimension of microstructure characterization. Metall. Mater. Trans. A 39, 374.

Zambaldi, C., Raabe, D., 2010. Plastic anisotropy of γ-TiAl revealed by axisymmetric indentation. Acta Mater. 58, 3516.

Zhu, T., Li, J., Van Vliet, K.J., Ogata, S., Yip, S., Suresh, S., 2004. Predictive modeling of nanoindentation-induced homogeneous dislocation nucleation in copper. J. Mech. Phys. Solids 52, 691.

Ziegenhain, G., Urbassek, H.M., 2010. Nanostructured surfaces yield earlier: molecular dynamics study of nanoindentation into adatom islands. Phys. Rev. B 81, 155456.

Ziegenhain, G., Hartmaier, A., Urbassek, H.M., 2009. Pair vs many-body potentials: influence on elastic and plastic behavior in nanoindentation of fcc metals. J. Mech. Phys. Solids 57, 1514–1526, http://dx.doi.org/10.1016/j.jmps.2009.05.011.

Ziegenhain, G., Urbassek, H.M., Hartmaier, A., 2010. Influence of crystal anisotropy on elastic deformation and onset of plasticity in nanoindentation: a simulational study. J. Appl. Phys. 107, 061807.

Zimmerman, J.A., Kelchner, C.L., Klein, P.A., Hamilton, J.C., Foiles, S.M., 2001. Surface step effects on nanoindentation. Phys. Rev. Lett. 87, 165507.